In-orbit performance of the ISO Long Wavelength Spectrometer

Bruce. M. Swinyard[a], Martin J. Burgdorf[b], Peter E. Clegg[c], Gary R. Davis[d], Matthew J. Griffin[c], Cecile Gry[b], Sarah J. Leeks[c], Tanya L. Lim[b], Stefano Pezzuto[b], Elisabetta Tommasi.[b]

[a]Rutherford Appleton Laboratory, Chilton, Didcot, Oxon, OX11 0QX, U.K.
[b]LWS Instrument Team, ISO Science Operations Centre, P.O. Box 50727, 28080 Madrid, Spain.
[c]Queen Mary and Westfield College, University of London, Mile End Road, London, E1 4NS, U.K.
[d]University of Saskatchewan, 116 Science Place, Saskatoon, Sask., S7N 5E2, Canada.

1. ABSTRACT

The long wavelength spectrometer (LWS) on-board the European Space Agency Infrared Space Observatory (ISO) uses a grating and one of two Fabry-Perot interferometers to make medium ($\lambda/\Delta\lambda \sim 200$) and high ($\lambda/\Delta\lambda \sim 10000$) resolution spectroscopic observations in the 43-196.9 μm wavelength range. The instrument has been in continuous use since the launch of ISO in November 1995. In this paper we describe the calibration of the instrument and its performance, both spectroscopic and photometric, over the two years of instrument operations.

Keywords: Instrumentation, far infrared, spectrographs, space

1. INTRODUCTION

The European Space Agency (ESA) Infrared Space Observatory (ISO) was launched on November 17th 1995. It carries four instruments that between them cover the wavelength region from 2.5 to 240 μm with a complementary mix of imaging and spectroscopic capabilities[1]. The long wavelength spectrometer (LWS) is designed to make medium resolution spectroscopic measurements ($\lambda/\Delta\lambda \sim 200$) in the relatively unexplored wavelength range between 43 and 196.9 μm in order to detect the astrophysically important lines of atomic and molecular species found in this range, and to search for broad emission features associated with solid state transitions from cool dust. In order to determine the velocity structure within a source and detect faint lines against a strong continuum, a high resolution capability ($\lambda/\Delta\lambda \sim 10000$) is also provided. In an earlier paper we reported on the initial results of the in-orbit calibration and performance evaluation[2], in this paper we discuss the long term performance and calibration of the instrument and update the performance figures. The instrument and its operation are briefly described, an overview of the instrument in-orbit calibration is given and the performance of the instrument sub-systems over the more than two years of operations is discussed in detail. An error budget for the instrument calibration is given and the in-orbit performance compared to that predicted from pre-launch calibration.

2. INSTRUMENT DESCRIPTION AND OPERATION

The cold focal plane unit (FPU) of the LWS consists of a grating spectrometer working in first order to cover from 84 to 196.9 μm and second order to cover from 43 to 93 μm; two Fabry-Perot interferometers covering respectively 47 - 70 μm and 70 - 196.9 μm; and collimating and re-imaging optics to focus the beam onto a detector sub-system that consists of ten doped germanium photo-conductors. The resolution of the grating at the centre of the grating movement is 0.6 μm in first order and 0.29 μm in second. The Fabry-Perots are mounted on an interchange wheel that allows the selection of one or the other or for the beam to pass through an aperture for grating only observations. The grating performs the order sorting function for the Fabry-Perots and the grating is order sorted using broad band filters mounted in front of the detectors. There are five detectors covering the grating first order, each with a pass band of approximately 20 μm, and five covering the second order each with a pass band of approximately 10 μm.

The detector pass bands are designed to prevent the detection of higher, unwanted, orders from the grating whilst allowing a significant overlap between adjacent detectors. Three types of detector are used: Ge:Be for the shortest wavelength channel (43 to 50 μm), denoted SW1; unstressed Ge:Ga for the five channels covering 50 to 110 μm, denoted SW2, SW3,

SW4, SW5 and LW1 respectively; and stressed Ge:Ga for the four channels covering 110 to 196.9 μm, denoted LW2, LW3, LW4 and LW5. The Ge:Be and unstressed Ge:Ga detectors are operated at 3.0 K and the stressed Ge:Ga at 1.8 K. All ten detectors are read out using JF-4 integrating amplifiers supplied by Infrared Laboratories, Inc. The outputs of the integrating amplifiers are sampled at 88 Hz and the amplifiers reset at 0.25, 0.5 or 1 second intervals. The relative response of each detector is monitored using infrared illuminators also supplied by Infrared Laboratories, Inc. A full description of the instrument and its operation is given in Clegg *et al.*[3]

The instrument has two basic modes of operation: the grating mode and the Fabry-Perot mode. In the grating mode the interchange wheel is set to provide a clear aperture and the grating is rotated about its central axis by means of a servo controlled drive mechanism. The scan range is determined by the wavelength range required for the particular observation; to scan the entire wavelength range of the LWS a rotation of $\pm 7^{o}$ is required. In Fabry-Perot mode the interchange wheel is used to place one or other of the Fabry-Perots in the collimated part of the beam through the instrument. The grating is set to a position commensurate with the central wavelength of the spectral region to be observed and the Fabry-Perot is scanned over a fixed wavelength range. To maximise the instrument transmission, the wavelength range covered at any one grating position is less than half the width of the grating response function. Therefore, to cover a wider wavelength range, the grating is moved in small steps and the Fabry-Perot scanned at each grating position. Section 4.5 gives a more detailed explanation of how the Fabry-Perots are used for measuring resolved spectral features and continuum emission.

3. OVERVIEW OF INSTRUMENT CALIBATION AND DATA PROCESSING

Before we discuss the detailed calibration for each of the instrument sub-systems, it is necessary to discuss briefly the procedures used for processing the instrument data, as it is these that, to some extent, determine how and why the calibration was carried out. The data processing is divided into two distinct stages:

1. The conversion of the raw digitised signal from the detectors and mechanisms into photocurrent at each mechanism position - this stage is termed Derive SPD (Standard Processed Data).

2. The conversion of mechanism position into wavelength and photocurrent in absolute flux units - this stage is termed AA (Auto Analysis).

The conversion between raw digitised signal and engineering units was established during ground testing and verified in the early phase of the ISO mission. The first stage of processing therefore requires little or no astronomical calibration. The major exception to this is the case of the correction applied for detector non-linear response when observing very bright sources.

The relationship between flux and photocurrent in grating mode has been established using observations of Uranus and a model Uranus spectrum[2,4] (see section 4.4). This calibration observation was carried out at a fixed time in the mission. All previous and subsequent observations are referred to the photocurrent to flux relationship derived from Uranus by taking the ratio between the signal measured when the illuminators are operated during an observation, and that measured when they were operated during the calibration observation of Uranus. To ensure that the power from the illuminators has not changed during the course of the mission, weekly observations have been made of a series of astronomical sources and the signal from these compared to that from the illiminators[5]. The Uranus data are also used to establish the response of the instrument as a function of wavelength in grating mode - the Relative Spectral Response Function or RSRF. This is tabulated and stored as a calibration file. The basic conversion between photocurrent and flux for all LWS data is carried out using this calibration file. The implications of this approach for the accuracy and repeatability of the LWS calibration are discussed in Lim et al[5] and section 5 below.

The flux calibration in Fabry-Perot mode is more complex than for the grating. Ideally the relationship between photocurrent and flux for the Fabry-Perots would have been directly established using observations of sources with known spectral characteristics. However, the transmission of the Fabry-Perots is such that only the very brightest objects (Jupiter and Saturn) would have made suitable candidates for such observations. These have relatively poorly known far infrared

spectra and, even with sources as bright as these, the observations would have been prohibitively long. Therefore a boot strap method is used whereby the photocurrent is first converted to flux using the grating mode relationship and the signals from the illuminator operations, this also removes the signature of the instrument RSRF in grating mode. The transmission of the Fabry-Perot as a function of wavelength is then accounted for in a separate processing stage. The signature of the grating response profile also has to be removed in a separate operation. The limitations of this approach are discussed in section 4.5.

The pipeline processing of the LWS data makes no attempt to correct for angular response of the instrument, i.e. the beam shape, or for any anomalous instrument behaviour such as the channel fringing seen on the measured spectra of extended or off-axis sources and the stray-light features seen for certain classes of object. The pipeline processing therefore only derives the true flux for point like sources at the centre of the LWS field of view. A full description of the pipeline processing and its performance is given by Burgdorf *et al.*[6]

4. INSTRUMENT PERFORMANCE AND CALIBRATION

4.1 GRATING WAVELENGTH CALIBRATION

The wavelength calibration of the LWS grating mode was determined and is monitored by measuring strong emission lines from a number of targets chosen as wavelength standards. The wavelength targets are mainly planetary nebulae, such as NGC6543, and HII regions, such as S106. These sources have been chosen so as to provide the largest possible sample of lines and so that several of them are visible from ISO at any given revolution*. The observations are performed weekly with end-to-end grating scans. Seven emission lines are observed, spread between 51 μm and 158 μm and appearing within the pass-band of two detectors each.

The wavelength is determined by the angle at which the grating is rotated and by the angle between the direction of the input beam onto the grating and the detector aperture - this is a constant known as the "detector angle". Once the ten detector angles are known, the wavelength calibration consists in finding the relationship between the output of the grating position monitor (this is an LVDT; Linear Voltage-Displacement Transducer) and the actual grating angle. This relationship is in principle independent of the detector used so that all measurements of all lines can be included in its determination. A third order polynomial fit is used between the grating angle and LVDT that allows, in principle, for a highly accurate determination of any unknown wavelength. However, repeated measurements of the same lines show that the repeatability of the grating servo system only allows the determination of the wavelength of an unknown line to within one quarter of a resolution element. The differences between expected wavelengths and wavelengths derived from the LVDT with an initial polynomial relationship, showed systematic offsets between some

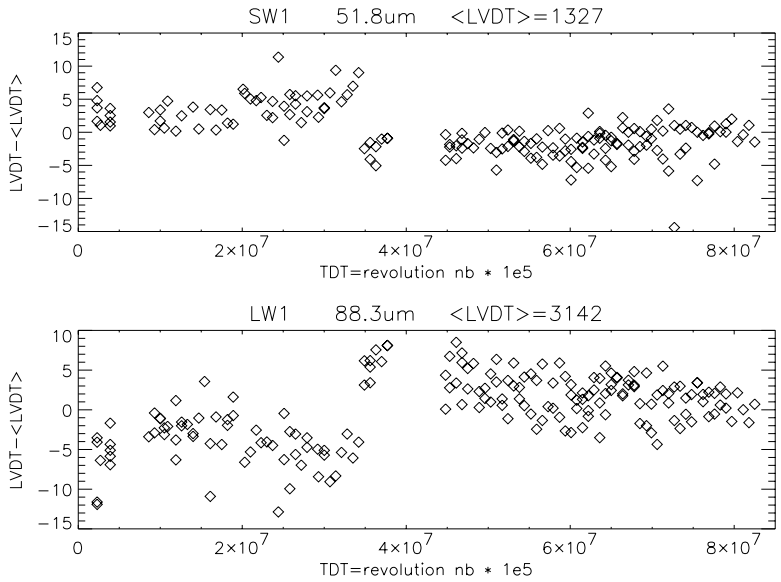

Figure 1: Deviation of the measured line centre (in engineering units from the LVDT) from the average value as a function of time for two lines recorded at opposite grating angles relative to the rest position (LVDT~2100). 40 LVDT units corresponds to 1 resolution element of the grating. Between revolutions 378 and 442 no observations were performed with the LWS because of a problem with the FP interchange wheel.

* A revolution is the term used for time period between one perigee passage of the satellite and another - this is nominally 24 hours for ISO.

detectors. This suggested that some of the detector angles had changed after launch and their values have been slightly adjusted to minimise the offsets for all detectors.

The stability of the system is checked by monitoring the measured LVDT at the line centres in the weekly observations. It is found to be stable for measurements performed close to the rest (zero drive current) position of the grating. But at positions away from the rest position a small discontinuity is seen in revolution 346. The discrepancy is larger the farther the grating is from the rest position, and has opposite signs for opposite grating angles (see figure 1). In the worst case, the discrepancy is less than half of a resolution element.

The discontinuity implies that the relationship between grating angle and LVDT reading changed on revolution 346 for some unknown reason. It was, therefore, decided to derive a time-dependent wavelength calibration which, at present, applies to two distinct periods - before and after revolution 346. After revolution 346, only a very slow drift is observed in the LVDT measurements. The new time-dependent wavelength calibration has been tested on independent targets and these measurements confirm the nominal accuracy value of a quarter of a resolution element.

4.2 FABRY-PEROT WAVELENGTH CALIBRATION

The LWS contains two Fabry-Perot interferometers, denoted FPS (47-70um) and FPL (70-197um). Their design was fully described by Davis et al.[7]. They use free-standing, inductive metal meshes as the reflecting elements: one is fixed while the other is mounted on a moving plate, which is driven against a set of leaf springs by moving-coil actuators to provide the spectral scanning capability.

The relationship between the gap between the Fabry-Perot etalons and the digital commanded value to the servo mechanism has been found to be well represented by a cubic. The objectives of the wavelength calibration are to determine the coefficients of this relationship and to monitor their drift with time during the mission. The calibration is performed using a number of astronomical spectral lines of known wavelengths, which span a sufficient range of gap and wavelength values to adequately sample the parameter space (table 1). The centroid of the measured response versus commanded position is taken to correspond to the line centre.

The calibration was tested against a separate set of sources to those used for the primary calibration and appears to be accurate to within half a resolution element. Repeated measurements of a number of sources have been carried out throughout the ISO mission. These show that the calibration is stable in time, although there does appear to be some evidence of small systematic offsets between the expected and derived wavelengths in some sources (see table 1); work is in progress to clarify these and to improve the accuracy.

	Source Name (literature velocity)			
Species and rest wavelength (μm)	NGC 7538 (-60.8)[8]	G0.6-0.6 (16.6)[9]	NGC 7027 (24.0)[10]	NGC 7023 (3.7)[11]
OIII(51.81450)	-	12.5±1.1	22.6±2.4	-
OI(63.183705)	-62.5±4.0	-	28.6±1.2	4.2±2.1
OIII(88.3560)	-40.5	27.75± 0.61	-	-
NII(121.897570)	-	11.1±1.1	-	-
OI(145.525439)	-	-	38.0±1.7	16.2± 2.6
CII(157.74090)	-53.09± 0.72	-	27.5±1.5	3.6±2.2

Table 1: The mean velocities with respect to the local standard of rest measured for the LWS standard calibration sources from repeated observations over the lifetime of the ISO mission. All values are in km/s; as a comparison the width of the Fabry-Perot resolution element is about 30 km/s. In addition to the species listed here, the NIII(57.34) line was also used for calibration

4.3 EXTRACTION OF PHOTOCURRENT

As mentioned in section 2, the cold read out electronics for the detectors use Infrared Labs JF-4 integrating pre-amplifiers. The photocurrent from a detector causes a charge build up on the integrating node of its amplifier, producing a voltage ramp which represents the input flux. This charge build up leads to a drop in the net bias voltage across the detector. As the bias voltage changes, so the resistance and responsivity of the detector also change. At high fluxes this causes the ratio between the derived photocurrent and the input flux to change as a function of input flux - i.e. the system becomes non-linear.

The original method of extracting photocurrents from integration ramps[12] assumed that the detector's intrinsic response is linear and that a simple model of the behaviour of the detectors in conjunction with the JF-4s could be used to account for changes in responsivity as function of bias voltage. The photocurrent was extracted by using a first or second order polynomial fit to the voltage ramps. A first order fit was used when the total voltage change at the end of the ramp was small, but second order fits were required for larger changes. This order swapping introduced an undesirable discontinuity in the calibration.

An empirical method for the derivation of the photocurrent, and hence flux, from the voltage ramps has been devised that avoids the problem of deciding on which degree of polynomial should be fitted. In this method the net change in the output voltage of the pre-amplifier is calculated by taking the difference in the output voltage at two fixed times in the reset period: for a 0.5 second reset these are at 0.055 and 0.49 seconds - sample number 6 and 43 out of 44. This voltage difference is divided by the time between the samples to give the rate of change of the voltage which can then be converted to current knowing the input capacitance of the pre-amplifier. The flux is then derived by reference to the observations of Uranus as described above. This method makes no *a priori* assumptions about how the detectors respond, but produces well calibrated spectra with no discontinuities due to processing and, it has been found, with lower net noise in the reduced spectra.

4.4 FLUX CALIBRATION IN GRATING MODE

The LWS flux and relative spectral response (RSRF) calibration is derived from a 5.7 hour observation of Uranus obtained in revolution 317 on the 28th September 1996. This observation consisted of 36 end to end grating scans interleaved with dark current measurements. The whole observation was followed by a series of illuminator operations to establish the baseline for correcting any drift in detector responsivity with time (see section 3)

For the LWS it is difficult to test the accuracy of the absolute flux calibration due to a lack of trustworthy model spectra in this wavelength range. However, comparisons can be made with stars with an FIR excess (Arcturus and Aldebran); with other planets (Neptune and Mars - Jupiter and Saturn are too bright and Venus is too close to the sun) and with asteroids such as Ceres. As each of the ten LWS detectors is calibrated separately for each observation, the accuracy of each detector is determined individually. Figure 2 shows the full LWS spectra of four objects: Mars; Ceres; Neptune and Arcturus, plotted together with model spectra. These examples cover the flux range observable by LWS.

Generally, over the whole dynamic range of LWS for these point sources there is a good agreement with the models. For Ceres, which has a similar flux to Uranus, there is good agreement with the model of Meuller[13] except at the longest wavelengths where the LWS spectrum is slightly steeper. For Neptune, the model of Lellouch[14] shows an upward deviation from the LWS data below 70 μm, but there is good agreement beyond 80 μm. This possibly indicates some error in the model Uranus spectrum used for calibration, although there is some disagreement between various models of Neptune in the shorter wavelength range. Also other source spectra do not show a discrepancy as large as that indicated by this Neptune model.

The observation of Arcturus is affected by two problems: the source flux for most detectors is less than the dark current, making uncertainties in the determination of the dark current critically important to the accuracy of the derived flux, and the observation is affected by near infrared filter leaks. How-so-be-it, there is a general agreement with the model of Cohen et al.[15] Observations of Aldebran and Sirius are planned to further confirm the calibration of the LWS against this important group of sources.

For Mars there is a general agreement with the model of Orton and Griffin[16] except for detectors LW3 and LW4. These detectors are non-linear in this regime and must be corrected for this before comparison with the models. The model of Mars used for this comparison is based on an extrapolation of the model provided by Wright[17] for the JCMT "FLUXES" program, and, as such, is liable to some error in the short wavelength region. This may partly account for the differences between the model and the derived spectrum in this region, although this may again be an indication of an error in the Uranus model at the short wavelength end of the LWS band.

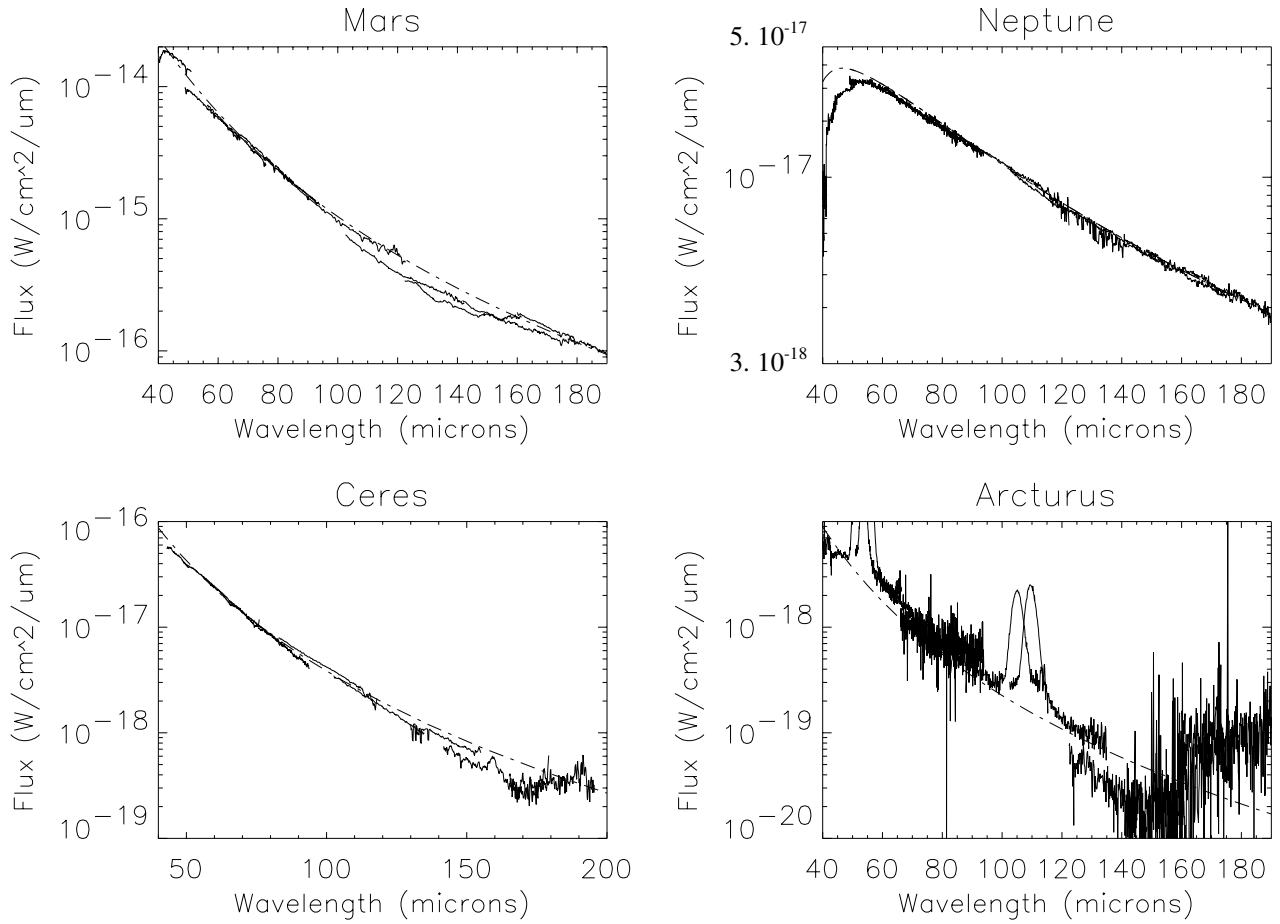

Figure 2: Measured LWS grating spectra of Mars, Neptune, Ceres and Arcturus plotted with the models described in the text. The anomalous features seen in the spectrum of Arcturus are due to near infrared leaks through the detector pass-band filters.

4.5 FLUX CALIBRATION IN FABRY-PEROT MODE

As discussed in section 3, we have adopted a bootstrapping calibration procedure for the Fabry-Perots in which we extend the grating-mode flux calibration to include two other factors: the grating response profile and the interferometer efficiency. Measurements of the Fabry-Perot efficiency and resolving power were made during ground testing using a far infrared laser at a number of spot wavelengths[18]. It has proved difficult to confirm these measurements in orbit owing to an absence of emission lines that are sufficiently narrow such that the intrinsic width of the line can be ignored with respect to the resolution element of the Fabry-Perot. At present the values of both the efficiency and the resolution element width derived from ground testing are used for the calibration of Fabry-Perot data.

Fabry-Perot observations with the LWS are implemented as a series of miniscans. For each miniscan, the grating is set to a fixed position and the selected interferometer is scanned over a range of gap values. At the end of the interferometer scan, the grating is moved to a different position and the next miniscan begins. Each miniscan therefore samples the grating response profile, which must also be removed from the data.

Removal of the grating response profile has proved difficult because of non-repeatability of unknown origin in the grating position (section 4.1). For high-resolution observations this non-repeatability corresponds to an uncertainty in the wavelength at which the grating profile is centred. The standard pipeline processing takes no account of this uncertainty: it assumes that the grating response profile is centred at exactly the wavelength specified by the grating wavelength calibration. When the grating profile is removed from the Fabry-Perot data, the result can be a spectrum that is

significantly skewed. The unpredictable nature of the grating setting, combined with the fact that there is no independent means of determining the grating position, means we are forced to infer the grating position directly from the data

An algorithm has been developed that minimises the sum of the squares of the differences between the overlapping portions of a mini-spectrum and its neighbours on either side as a function of the position of the underlying grating profile. The only free parameter for each mini-spectrum is the grating position, and there is only one criterion; namely, that the fluxes measured on overlapping portions of a mini-spectrum must agree. The procedure is applied to each mini-spectrum in turn and is repeated for the whole spectrum until the maximum shift in any one grating position is insignificant compared to the width of the Fabry-Perot resolution element.

The non-repeatability in the grating position also leads to a second problem. If the grating profile is sufficiently shifted in wavelength from its commanded position, then Fabry-Perot interference orders adjacent to the selected one can make a significant contribution to the measured flux. This spectral contamination is potentially important at the shortest wavelengths of each Fabry-Perot wavelength range. When both effects are present, they are difficult to remove simultaneously.

4.6 DARK CURRENT DETERMINATION

The dark current has been determined by three independent methods:

1. Two long measurements of the dark background were taken with the one of the Fabry-Perots in the beam with its etalons set non-parallel. The first measurement was taken straight after the mid-revolution detector curing procedure[5] and the second in the last hour before the close of the LWS science window[19].

2. Routine checks of the dark current are made near apogee in every revolution to monitor long term trends in the detector behaviour[5]. As no long term drifts are found in the value of the dark currents, these measurements can be combined to obtain an independent determination of the dark signal.

3. When the LWS is not the prime instrument, useful data can still be obtained by recording the output of the detectors with low time resolution. Much of the time during these *serendipity mode* operations the LWS is viewing blank portions of the sky and the data can be used to determine the detector dark currents.

The results of the three independent means of measuring the dark currents are given in table 2. They agree with each other to within one or two standard deviations. The low values for some detectors seen in the serendipity mode derivation are probably due to the lack of sampling of the pre-amplifier output and the different method used for deriving the photocurrent. The higher values derived from the hand-over illuminator operation reflect the fact that these are measured

Detector	Type	Measured in dedicated long observations in revolution 650		Measured during apogee illuminator operations	Measured from serendipity mode
		Mid-revolution	End of revolution		
SW1	Ge:Be	4.89±0.42	4.96±0.53	5.68±1.82	4.98±0.58
SW2	Ge:Ga(u)	2.15±0.38	2.11±0.40	2.42±1.20	1.98±0.32
SW3	Ge:Ga(u)	2.23±0.19	2.31±0.20	2.58±0.86	2.00±0.23
SW4	Ge:Ga(u)	1.21±0.30	1.25±0.30	1.32±0.40	0.89±0.24
SW5	Ge:Ga(u)	1.63±0.21	1.67±0.22	1.72±0.27	1.35±0.22
LW1	Ge:Ga(u)	2.39±0.27	2.63±0.28	2.77±0.53	2.26±0.30
LW2	Ge:Ga(s)	0.10±0.22	0.17±0.23	0.42±0.36	0.17±0.18
LW3	Ge:Ga(s)	0.49±0.32	0.49±0.34	1.20±1.03	0.39±0.25
LW4	Ge:Ga(s)	2.23±0.38	1.94±0.38	2.52±1.44	1.84±0.33
LW5	Ge:Ga(s)	1.40±0.22	1.18±0.22	1.28±0.35	0.98±0.25

Table 2: Derived values of the detector dark currents from three independent measurements. Units are 10^{-16} A in all columns and the uncertainties are quoted as one standard deviation.

Detector	Centre wavelength (μm)	Responsivity (A cm^2 μm W^{-1})	Estimated noise for 0.5 sec resets (10^{-17} A)	NESD (10^{-19} W cm^{-2} um^{-1} $Hz^{-1/2}$)	New NEFD (10^{-19} W cm^{-2} $Hz^{-1/2}$)	Telescope effective area (cm^2)	Estimated instrument NEP (10^{-16} W $Hz^{-1/2}$)	NEP from ground tests (10^{-16} W $Hz^{-1/2}$)
SW1	46.1333	94.2	4.17	4.43	1.28	2459.87	3.16	0.690
SW2	56.1141	49.4	3.83	7.75	2.25	2431.59	5.47	2.02
SW3	66.029	63.8	1.91	3.00	0.871	2346.77	2.04	0.610
SW4	75.613	55.1	2.98	5.40	1.57	2261.95	3.55	0.543
SW5	84.6776	49.7	2.13	4.28	1.24	2205.40	2.74	0.531
LW1	102.246	315.7	2.68	0.849	0.509	1922.65	0.980	0.302
LW2	122.039	977.3	2.26	0.231	0.138	1837.83	0.254	0.129
LW3	141.634	2607.8	3.19	0.122	0.0734	1837.83	0.135	0.0640
LW4	160.385	1896.4	3.83	0.202	0.121	1753.01	0.212	0.120
LW5	177.737	320.4	2.21	0.691	0.414	1583.36	0.656	0.0755

Table 3: The estimated sensitivity of the LWS instrument in-orbit. The last two columns provide a comparison between the predicted performance on the ground in quiescent laboratory conditions and an estimate of the in-orbit performance based on model values of the effective area of the ISO telescope.

with a short integration time (8 seconds) and are therefore prone to problems of contamination by radiation hits. It is noteworthy that there appears to be no significant change in the level of the dark current between the middle and end of a revolution. This is in disagreement with predictions from tests made during pre-launch calibration[20].

4.7 DETECTOR PERFORMANCE

The sensitivity of the LWS instrument in terms of Noise Equivalent Spectral Density (NESD) and Noise Equivalent Flux Density (NEFD) can be calculated given an estimate of the detector noise with zero background power and a measurement of the instrument responsivity. This can be converted to Noise Equivalent Power (NEP) for the instrument if the effective area of the ISO telescope is known. The detector noise can be estimated from the uncertainties in the dark current measurements taken on revolution 650 (see section 4.6) and the instrument responsivity from the observations of Uranus. It is more difficult to know the exact value of the ISO telescope effective area given the problems encountered with interpreting the measurements of the LWS beam (see section 4.9). However, the model values can be used as an estimate in order to facilitate a comparison between ground and in-orbit instrument NEPs.

Inspection of table 3 shows that the instrument NEPs have increased by an average of a factor of four. About half of this increase is due to the use of 0.5 second amplifier resets rather than the 2 second resets used in ground testing - the noise is proportional to the square root of the reset time up to resets of about 4 seconds[9]. This change was forced upon us by the debilitating effect of charged particle hits on the detectors. The responsivity of the detectors is also reduced in orbit because the bias voltage has been reduced, again due to the effects of charged particles.

4.8 RESPONSE TO OFF-AXIS AND EXTENDED SOURCES

Channel fringes are seen on all LWS spectra of extended or off-axis point sources[2]. Extensive modelling of the response of the instrument has been carried out using the ASAP™ optical design software. This has shown that the channel fringing is caused by interference between the reflecting surface of the LWS field mirror and its support structure as the diffraction pattern from the source falls off the edge of the field mirror itself. The reflectivity of the support structure material is not well known at these wavelengths and, although the model gives a qualitative explanation of the phenomenon, it has not, so far, been possible to produce an exhaustively quantitative model that would allow the removal of the channel fringes given knowledge of the spatial structure of the source. Instead a method has been devised that performs a multivariate fit for the period, amplitude and phase of the sinusoid in wavenumber space and removes it from the spectrum by division or subtraction. This has proved successful in removing the channel fringing from the continuum spectrum of most sources whilst preserving the shape and intensity of the unresolved spectral features.

Wavelength (μm)	Beam FWHM "Y" - direction (arcsec)	Beam FWHM "Z" - Direction (arcsec)
46.1333	80.8	70.6
56.1141	79.9	77.3
66.029	81.5	84.5
75.613	80.5	79.7
84.6776	83.5	76.0
102.246	78.3	69.9
122.039	78.1	74.9
141.634	69.5	65.2
160.385	71.5	70.1
177.737	69.3	69.2

Table 4: The LWS beam FWHM for the integrated flux from Mars over each detector pass-band. The statistical uncertainty on the measurements is estimated as no more than ± 1 arcsec; however, these results should be treated as preliminary only as there may be some systematic uncertainties still associated with them. The Y and Z directions refer to the ISO telescope co-ordinate system

4.9 INSTRUMENT FIELD OF VIEW

The spatial response of the LWS in conjunction with the ISO telescope has been measured using Mars. End to end grating scans were taken with Mars placed at different positions with respect to the optical axis of the LWS. In particular, these observations have allowed the beam profile to be determined in two orthogonal directions with respect to the optical axes of the LWS as a function of wavelength. The data have been reduced by taking the total area under a scan for each pointing and normalising this to the on-axis observation. This analysis gives an accurate measurement of the beam profile for the central wavelength of each detector band. Table 4 gives the measured full width at half maximum (FWHM) of the, essentially Gaussian, beam profiles.

Several points are to be noted from this analysis:

1. The FWHM of the beam profile given in table 6 is rather narrower at all wavelengths than predicted by a simple convolution between the telescope diffraction pattern and the geometrical area of the field mirror - around 100 arcsec. Even a more sophisticated Fourier optics analysis predicts a beam FWHM of nearer 90 arcsec at 45 μm. A much more detailed analysis is now being carried using the ASAP™ optical design program that will take into account the clipping of the beam at all optical components[24].

2. The beam is asymmetric. This is a consequence of the field mirror being circular and placed at an angle to the optical path, thus giving an elliptical shape to the geometric field stop.

3. When the data are analysed as a function of wavelength over the whole LWS range, it is clear that the channel fringing seen on the spectra is also present in the FWHM of the LWS field of view. This is a natural consequence of the process that leads to the channel fringing.

5. CALIBRATION ERROR BUDGET

5.1 GRATING CONTINUUM FLUX ERROR ESTIMATION

The grating flux is given by:

$$F(\lambda) = \frac{P(\lambda) - D}{f_R R(\lambda)\, \Delta\lambda(\lambda)}, \qquad - 1$$

where $P(\lambda)$ is the photocurrent; D the dark current; f_R the responsivity correction factor from illuminator operation; $R(\lambda)$ detector responsivity from the RSRF (A cm^2 W^{-1}) and $\Delta\lambda(\lambda)$ the equivalent width of the grating resolution element at this wavelength.

We can write the uncertainty on this as:

$$\Delta F(\lambda) = \left(\Delta\left(\frac{P(\lambda)}{f_R R(\lambda)\, \Delta\lambda(\lambda)} \right)^2 + \Delta\left(\frac{D}{f_R R(\lambda)\, \Delta\lambda(\lambda)} \right)^2 \right)^{1/2}, \qquad - 2$$

where

$$\Delta\left(\frac{D}{f_R R(\lambda)\, \Delta\lambda(\lambda)} \right) = \left(\frac{\delta D^2}{D} + \frac{\delta f_R^{\,2}}{f_R} + \frac{\delta R(\lambda)^2}{R(\lambda)} \right)^{1/2} \text{x} \left(\frac{D}{f_R R(\lambda)\, \Delta\lambda(\lambda)} \right). \qquad - 3$$

All the parameters in equation (3) are known from the calibration data and the data from the observation itself. The dark current is measured on every observation as is the relative flux calibration. Typically $\delta D/D \sim 0.1$ and $\delta f_R/f_R \sim 0.05$. The quoted uncertainty in the Uranus model is 5% and the statistical error on the RSRF is better than 0.01. For observations where the dark current is not a significant contribution to the signal, the additional uncertainty contributed to the measurement by the calibration process is therefore of the order of 7% for most detectors. When the dark current becomes significant, i.e. when the last term in equation 3 becomes commensurate with the flux from the object itself, then the uncertainty in the measurement of the dark current begins to dominate. Long term monitoring has shown that the repeatability of the flux calibration is within 10% for all objects not influenced by the uncertainty in the dark current measurement[5].

5.2 FABRY-PEROT CONTINUUM FLUX ERROR ESTIMATION

For the Fabry-Perot the flux is given by:

$$F(\lambda) = \frac{P(\lambda) - D}{f_R R_g(\lambda)\, G(\lambda)\, \eta_{FP}(\lambda)\, \Delta\lambda_{FP}(\lambda)}, \qquad - 4$$

where, in addition to the definitions above, $R_g(\lambda)$ is detector responsivity in grating mode at this grating setting (the *RSRF* value in A cm^2 W^{-1}); $G(\lambda)$ the relative height of the grating resolution element profile at this wavelength; $\eta_{FP}(\lambda)$ the Fabry-Perot efficiency at this wavelength and $\Delta\lambda_{FP}(\lambda)$ the equivalent width of the Fabry-Perot resolution element at this wavelength (μm).

We can write the uncertainty on this as:

$$\Delta F(\lambda) = \left(\Delta\left(\frac{P(\lambda)}{f_R R_g(\lambda)\, G(\lambda)\, \eta_{FP}(\lambda)\, \Delta\lambda_{FP}(\lambda)} \right)^2 + \Delta\left(\frac{D}{f_R R_g(\lambda)\, G(\lambda)\, \eta_{FP}(\lambda)\, \Delta\lambda_{FP}(\lambda)} \right)^2 \right)^{1/2} \qquad - 5$$

where

$$\Delta\left(\frac{D}{f_R R_g(\lambda)\, G(\lambda)\, \eta_{FP}(\lambda)\, \Delta\lambda_{FP}(\lambda)} \right) = \left(\frac{\delta D^2}{D} + \frac{\delta f_R^{\,2}}{f_R} + \frac{\delta R_g(\lambda)^2}{R_g(\lambda)} + \frac{\delta G(\lambda)^2}{G(\lambda)} + \frac{\delta \Delta\lambda_{FP}(\lambda)^2}{\Delta\lambda_{FP}(\lambda)} + \frac{\delta \eta_{FP}(\lambda)^2}{\eta_{FP}(\lambda)} \right)^{1/2}$$
$$\times \left(\frac{D}{f_R R_g(\lambda)\, G(\lambda)\, \eta_{FP}(\lambda)\, \Delta\lambda_{FP}(\lambda)} \right), \qquad - 6$$

Although we are be in a position to place uncertainty estimates on the Fabry-Perot efficiency and resolution element width using a mixture of ground based data and calibration observations; the determination of the *systematic* uncertainties in the placement and shape of the grating resolution element are far more difficult. Instead, for continuum spectra at least, an estimate of the uncertainty in the flux level in the spectrum owing to both the inherent statistical fluctuations *and* any systematic error caused by the use of an incorrect grating profile or its incorrect position, can be obtained by averaging across all scans and all mini-spectra. This is very dependent on the nature of the spectrum and the signal to noise obtained in the measurement.

One method of estimating the total uncertainty in the Fabry-Perot efficiency and resolution element width is by comparison between spectra measured on both the grating and the Fabry-Perots. By this method it is estimated that the error on the product of the efficiency and the width of the resolution element is about 30%, i.e.

$$\left(\frac{\delta \Delta\lambda_{FP}(\lambda)^2}{\Delta\lambda_{FP}(\lambda)} + \frac{\delta \eta_{FP}(\lambda)^2}{\eta_{FP}(\lambda)} \right)^{1/2} \approx 0.3 . \qquad - 7$$

As with grating spectra, when the flux from the object is close to the equivalent flux from the dark current, i.e. when the last term in equation 6 is commensurate with $F(\lambda)$, then the uncertainties in the dark current determination will dominate.

5.3 ERROR ESTIMATION FOR ISOLATED LINES

The calculation of the estimated error in the flux of an isolated line is rather simpler than for the continuum if a baseline can be subtracted that represents the continuum level close to the line. The total flux at any point in a narrow line on a continuum is obtained from the photocurrent by:

$$F_{Line} = F_{Total} - F_{Cont.} = \left(\frac{P_C(\lambda) + P_L(\lambda) - D}{CF(\lambda)}\right) - \left(\frac{P_C(\lambda) - D}{CF(\lambda)}\right) = \left(\frac{P_L(\lambda)}{CF(\lambda)}\right), \qquad - 8$$

where: $P_C(\lambda)$ is the photocurrent arising from the continuum at this wavelength; $P_L(\lambda)$ is the photocurrent arising from the line at this wavelength; D is the dark current and $CF(\lambda)$ is the correction factor for the given instrument mode at this wavelength - i.e. the denominator in equation 1 for the grating and equation 4 for the Fabry-Perots.

That is, if one can subtract a fitted baseline that represents the continuum flux under the line, then the uncertainty estimation on the line flux is independent of the uncertainty in dark current and can be written as:

$$\Delta F_{Line} = \left(\frac{\delta F_{Line}(\lambda)^2}{F_{line}(\lambda)} + \frac{\delta f_R^{\,2}}{f_R} + \frac{\delta R(\lambda)^2}{R(\lambda)}\right)^{1/2} \text{x } F_{Line}(\lambda), \qquad - 9$$

for the grating, and:

$$\Delta F_{Line} = \left(\frac{\delta F_{Line}(\lambda)^2}{F_{Line}(\lambda)} + \frac{\delta f_R^{\,2}}{f_R} + \frac{\delta R_g(\lambda)^2}{R_g(\lambda)} + \frac{\delta G(\lambda)^2}{G(\lambda)} + \frac{\delta \Delta\lambda_{FP}(\lambda)^2}{\Delta\lambda_{FP}(\lambda)} + \frac{\delta t_{FP}(\lambda)^2}{t_{FP}(\lambda)}\right)^{1/2} \text{x } F_{Line}(\lambda), \qquad - 10$$

for the Fabry-Perots.

For isolated FP lines the systematic error arising from the removal of the grating profile remains problematic if the profile was not well centred as this a factor in the denominator. If the wings of the resultant line are symmetric after processing then it can be ignored.

6. CONCLUSIONS

The photometric calibration of the LWS is largely dependent on a single observation of Uranus and, consequently on the accuracy of the model spectrum applied to remove the Uranian signature. Whilst this approach appears to give a calibration better than 10-15% for moderately bright point like objects observed on axis, some questions remain over the accuracy of the model at short wavelengths. In the longer term it is planned that the calibration will be tied more closely to the Martian spectrum and extensive work is being carried out to cross calibrate the LWS with other instruments such as IRAS and the ISO photometer. The situation for extended objects is less clear owing to a lack of understanding of why the LWS beam is so much narrower than predicted by optical theory and the effect of the channel fringing on the flux calibration. The flux calibration obtained in the Fabry-Perot mode has not yet been fully analysed, although the first estimates show it to be better than 30% when compared to the grating observations.

The presence of ionising radiation in the space environment was anticipated and the effects on the photo-conductors tested during ground calibration. However, the effect of the ionising radiation on the detector performance has proved to be very much more deleterious than expected and has forced a change in the operating mode of the instrument. This has, in large part, lead to an increase in the instrument NEP of an average of a factor of four across the LWS wave-band.

The wavelength calibration of the grating has changed over the course of the mission, with a sharp discontinuity in the relationship between the position sensor and the true grating angle appearing after about one year of operations. The reason for this is not known, however continuous monitoring of the grating calibration has meant that a time dependent relationship can be applied that allows a wavelength calibration to within ¼ of the FWHM of the grating resolution element.

The wavelength calibration of the Fabry-Perot interferometers has remained stable throughout the mission. The wavelength calibration of the Fabry-Perots is within ½ of the FWHM of the resolution element, albeit that there are some, as yet, unexplained discrepancies between the observed and predicted wavelengths of lines from the sources used for monitoring the Fabry-Perot wavelength calibration.

The requirement set on the flux calibration for the LWS at the outset of the project was 30% in the grating mode and 50% in the Fabry-Perot mode. The requirement for the wavelength calibration was 1/5 of the FWHM in the grating mode and ½ of the FWHM in the Fabry-Perot mode. In most cases we have met the requirements set out for the instrument, in some areas problems remain and are the subject of further investigation.

7. ACKNOWLEDGEMENTS

ISO is an ESA project with instruments funded by ESA Member States (especially the PI countries: France, Germany, the Netherlands and the United Kingdom) and with the participation of ISAS and NASA. S. Leeks acknowledges the receipt of a U.K. Particle Physics and Astronomy Research Council grant.

8. REFERENCES

1 M. Kessler, *et al.*, "The Infrared Space Observatory (ISO) Mission", A & A **315**, pp L27-L31. 1996.
2 B. Swinyard, *et al.*, "Calibration and performance of the ISO Long-Wavelength Spectrometer", A & A **315**, pp L43-48. 1996.
3 P. Clegg, *et al.*, "The ISO Long-Wavelength Spectrometer", A & A **315**, pp L38-42. 1996.
4 M. Griffin and G. Orton, "The Near-Millimeter Brightness Temperature Spectra of Uranus and Neptune", ICARUS **105,** pp 537-547. 1993.
5 T. Lim, *et al.*, "Long term performance of doped Ge:Ga photoconductors in the space environment", in *Infrared Astronomical Instrumentation,* SPIE **3354**, in press. 1998
6 M. Burgdorf, *et al,* "Automatic data processing and quality control: experiences from ISO-LWS", in *Observatory Operations to Optimize Scientific Return,* SPIE **3349**, in press. 1998.
7 G. Davis, et al 1995, "Design and Performance of the Cryogenic, Scanning Fabry-Perot Interferometers for the ISO Long Wavelength Spectrometer", Appl. Optics **34**, p92. 1995.
8 F.J. Lockman, "A survey of radio HII regions in the northern sky", ApJS **71**, p469-479. 1989.
9 P.A. Shaver, R.X. McGee, L.M. Newton, A.C. Danks, S.R. Pottasch, "The galactic abundance gradient", MNRAS **204**, pp 53-112. 1983
10 S. Schneider, Y. Terzian, A. Purgathofer, M. Perinotto , "Radial velocities of planetary nebulae", ApJS **52**, p399-423. 1983.
11 L. Rogers, M.H. Heyer and P.E. Dewdney, "HI CO and IRAS onbservations of NGC7023", ApJ **442**, p694-713. 1995
12 S.E. Church, M.J. Griffin, P.A.R. Ade, M.C. Price, R.J. Emery, B.M. Swinyard, "Calibration and Performance of Doped-Ge Photoconductors for the ISO Long Wavelength Spectrometer", Infrared Phys. **34**, pp389-406. 1993.
13 T. Meuller, private communication, 1997
14 D. Lellouch, private communication, 1997
15 Cohen, Witteborn, Carbon, Davies, Wooden, and Bregman, "Spectral Irradiance Calibration in the Infrared.VII. New Composite Spectra, Comparison with Model Atmospheres, and Far-Infrared Extrapolations", AJ **112**, p2274, 1996
16 G. Orton and M. Griffin, private communication, 1997
17 E. Wright, private communication, 1996
18 R.J. Emery, K.J. King, B.M. Swinyard, S.E. Church, "Testing the Long Wavelength Spectrometer for ISO", in *Infrared Detectors and Instrumentation,* A Fowler, Editor, SPIE **1946***,* pp 272-280. 1993.
19 K. King, D. Ewart, D. Texier, "Life enhancement possibilities of trend analysis", in *Observatory Operations to Optimize Scientific Return,* SPIE **3349**, in press. 1998.
20 M. Price, M. Griffin, S. Church, A. Murray, P.A.R. Ade, "Ionising Radiation-Induced Effects in Doped Germanium FIR Photoconductors", *Proc. of ESA Symposium on Photon Detectors for Space Instrumentation,* ESA SP-356, pp309-312. 1992.
21 M. Caldwell, B. Swinyard, P. Gray, "The effect of multiple beam clipping in FIR and sub-millimetre instrumentation: ISO-LWS and FIRST-SPIRE. Submitted to SPIE conference on *Stray-light and System Optimisation*, San Diego. 1998.